EXPERIMENTAL ANALYSIS ON SHEAR BEHAVIOR OF REINFORCED CONCRETE BEAMS BASED ON COMPRESSIVE FORCE PATH METHOD

ERGANG XIONG[1]* **, KUN ZU**[1]**, TUANJIE FAN**[1]**, LINBO LIU**[1] **, LIANGYING SONG**[1] **, QIAN ZHANG**[2]
[1]School of Civil Engineering, Chang'an University, Xi'an 710061, China.
[2]School of Architecture and Engineering, Xi'an Eurasia University, Xi'an 710065, China

This paper attempts to disclose the shear behavior of reinforced concrete (RC) beams designed by compressive force path (CFP) method. For this purpose, three beams were designed by the CFP method and another three by GB 50010-2010. For each type of beams, the three beams were prepared with different shear span ratios, respectively 2.0, 1.5 and 1.0. Then, a monotonic loading test was performed on all the beams. To identify the effect of shear span ratio on shear behavior, the author compared the CFP beams with GB beams in terms of ultimate load, failure process and failure mode. In addition, the load-deflection curve and load-strain curves of concrete, reinforcement and stirrups were analyzed in details. The results show that the shear capacity of RC beams is mainly affected by the stress transmitted along the CFP; Compared with the GB method, the CFP method, despite using fewer number of stirrups, effectively guaranteed the shear capacity of the beams with any of the three shear span ratios, and did not significantly change the ultimate load; the amount of stirrups saved by the CFP is negatively correlated with the shear span ratio of the beam. To sum up, the CFP method was proved as a feasible and rational way to design RC beams.

Keywords: Compressive Force Path Method; Shear Capacity; Shear Span Ratio; Mechanical Properties; Stirrup

1. Introduction

There are many theories on the shear failure of reinforced concrete (RC) members, ranging from truss theory, limit equilibrium theory, plasticity theory, compressive force path (CFP) theory to nonlinear finite-element analysis theory. However, none of these theories can fully reflect the extremely complex shear mechanism of RC beams, such as the redistribution of internal forces after concrete cracking [1-3]. This calls for rational and practical theories on the calculation of shear capacity [4].

Proposed by Kotsovos in 1988, the CFP theory [5] suggests the existence of a transmission path for the compressive stress between the compression zone and the support of the beam. The shear mechanism of a RC member in the limit state can be interpreted from the angle of the CFP: the shear failure is the result of the cumulative tensile stress vertical to the cracks on the CFP [6]. Kotsovos [7, 8] explored the shear failure mechanism and shear capacity of RC members through experiments on different stirrup positions, indicating that the shear capacity is greatly affected by the stirrup position; the experimental results also show that the main stress is borne by the relevant areas along the CFP, rather than the dowel action of longitudinal reinforcement below the neutral axis and the aggregate interlock behavior, as believed in traditional theories. Both the CFP theory and the strut and tie model use the concept of force flow to describe the stress state of RC beams. The concept integrates the lower bound theorem into the plastic theory, making the theory more acceptable [9].

Based on the CFP theory, this paper designs three groups of RC beams with different shear span ratios, and investigates the mechanical properties of each group by the CFP method, in contrast to those of the beams per the *Code for Design of Concrete Structures* (GB 50010-2010) [10].

2. Materials and Methods

The main causes to shear failure of RC beams have been extensively explored to enhance the applicability of the CFP method. The existing studies have highlighted the close correlation between shear capacity and shear span ratio of RC beams [11, 12] and classified the failure modes into four categories (Table 1) [13].

Table 1

Classifications of failure modes

Failure Type	I	II	III	IV
a/d	5≤ a/d	2.5≤ a/d<5	1≤ a/d<2.5	a/d<1

As shown in Table 1, the type I failure mode mainly describes flexural failure; the type II failure mode shows the gradual transition to diagonal tensile failure, due to the large shear span; the type III failure mode deals with the shear span ratio of 1.0~2.5, and the shear capacity controlled by shear compression; the type IV failure mode involves the diagonal compressive failure of deep beams.

Among them, type III is the only failure mode that purely considers the shear behavior of RC beams. Hence, this paper takes type III failure mode as the object, and explores the shear behavior of RC beams with the shear span ratios of 2.0, 1.5 and 1.0.

2.1. Shear design of type III failure mode

Under the type III failure mode, the shear failure of a RC beam can be breakdown to the following steps: With the increase of load, oblique cracks gradually emerge in the shear span of the beam; At the occurrence of oblique cracks, the load is partially transmitted to the support via the compressive concrete, and the beam still has much of its bearing capacity; Once the main oblique cracks appear, the neutral axis height at the tip of the main cracks will decrease at the yield of the tensile reinforcements, pushing up the tensile stress in the compressive zone; Under the joint action of compression and shear, the compressive concrete will eventually surpass its bearing capacity, causing beam damages. Figure 1 illustrates the internal forces on the crack section of type III failure mode.
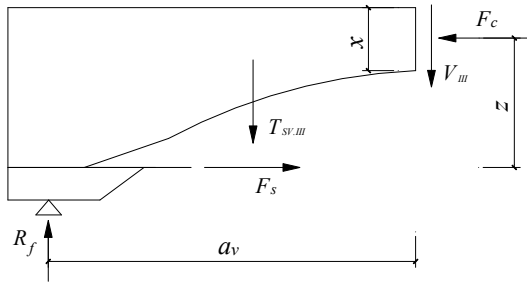

Fig.1 - Internal forces on crack section for type III failure mode.

Assuming that the stirrups on the crack section bear all the shear forces, and have all reached the yield state, the resultant force of stirrups in yield state $T_{sv.\mathrm{III}}$ equals the area of stirrups $A_{sv.\mathrm{III}}$ multiplying the yield strength of reinforcement f_{yv}. Considering the moment of the resultant force about its point of application in compressive concrete, the following formulas can be derived from bending moment equilibrium:

$$R_f a_v - T_{sv.\mathrm{III}}\left(a_v/2\right) - F_s z = 0 \qquad (1)$$

$$F_s z = M_{\mathrm{III}} \qquad (2)$$

$$M_f = \sigma_a b x \left(h_0 - x/2\right) \qquad (3)$$

where R_f is the reaction force at the support; a_v is the shear span length from the load action to the support; F_s is the tensile force of longitudinal reinforcement; z is the distance from the point of application to the tensile longitudinal reinforcement; V_{III} is the shear force; M_{III} is the bending moment at shear failure; M_f is the bending capacity of the beam; σ_a is the mean stress of compressive concrete; x is the height of compression zone; h_0 is the sectional effective depth.

The area of stirrups can be calculated by the equilibrium relationship in Figure 1:

$$A_{sv.\mathrm{III}} = 2\left(M_f - M_{\mathrm{III}}\right)/\left(a_v f_{yv}\right) \qquad (4)$$

The stirrups thus calculated should be arranged at the shear span with an interval of no more than 0.5 h_0. The interval requirement applies to both constructional and shear stirrups. The former should be able to bear a stress greater than 0.5MPa.

3. Experimental Program

3.1. Specimens

Three beams were designed by the CFP method and another three by GB 50010-2010. For each type of beams, the three beams were prepared with different shear span ratios, respectively 2.0, 1.5 and 1.0. Then, all the six beams were divided into three groups by the shear span ratio, such that each group has two beams with the same shear span ratio but designed by different methods. Each beam is 2,800mm in length, 2,400mm in net span and 150mm×300mm in sectional area. The longitudinal reinforcement adopts HRB400 reinforcement (diameter: 10mm), the nominal top reinforcement also uses HRB400 reinforcement (diameter: 22mm), while the stirrups employ HPB300 reinforcement (diameter: 6mm, 8mm and 10mm). In addition, the strength of the concrete belongs to the grade of C30. Table 2 list the loading point and the number of reinforcements in the beams. Figure 2 describes the reinforcement position and the arrangement of strain gauges (citing group B as the example). Since the strain gauges were arranged symmetrically, only the left side arrangement is provided in Figure 2.

(a) Layout of reinforcement and steel strain of beam B-1.5   (b) Layout of reinforcement and steel strain of beam B'-1.5.
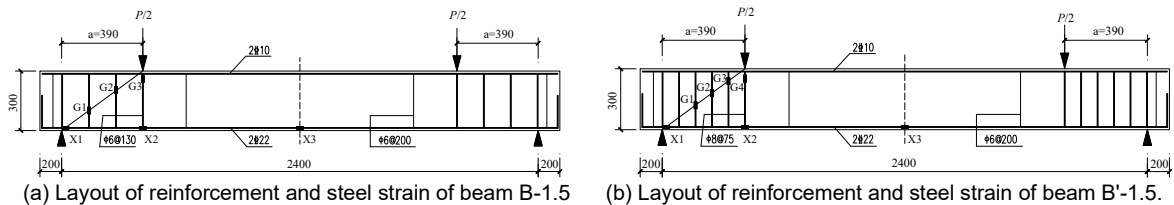Fig. 2 - Layout of reinforcement and strain gauges: X1, X2, X3 – The strain gauges placed on the support, loading point and midspan of the longitudinal reinforcements; G1, G2, G3, G4 – The strain gauges of stirrups from loading point to the support.

Ergang Xiong, Kun Zu, Tuanjie Fan, Linbo Liu, Liangying Song, Qian Zhang / Experimental analysis on shear behaviour
of reinforced concrete beams based on compressive force path method
603

Table 2

Basic parameters of specimens

Specimen	Reinforcement method	Shear span ratio	Loading location (mm)	Effective height (mm)	Longitudinal reinforcement	Shear reinforcement		Computation of constructional reinforcement	
						Number	Diameter /Spacing	Number	Diameter /Spacing
A-2.0	CFP	2.0	520	260	2Φ22	12	Φ6@100	2	Φ6@200
A'-2.0	GB	2.0	520	260	2Φ22	12	Φ8@100	2	Φ6@200
B-1.5	CFP	1.5	390	260	2Φ22	8	Φ6@130	2	Φ6@200
B'-1.5	GB	1.5	390	260	2Φ22	12	Φ8@75	2	Φ6@200
C-1.0	CFP	1.0	260	260	2Φ22	6	Φ6@130	4	Φ6@200
C'-1.0	GB	1.0	260	260	2Φ22	10	Φ10@50	4	Φ6@200

3.2. Loading plan and measurement

During the test, two concentrated loads were applied at two symmetric points, and the shear span ratio was adjusted by changing the position of the loading points. The specific loading plan was designed as per the *Standard for Test Method of Concrete Structures* (GB/T 50152-2012) [14]. Along the CFP of the shear span of each beam, strain gauges were arranged at an interval of 50mm on both sides, and another three strain gauges were arranged horizontally at the midspan along the vertical direction of the beam. These strain gauges are responsible for detecting the emergence of oblique cracks. Five deflection measuring points were set up at the two end supports, two loading points and the midspan of each beam. The displacement at each of the five points was measured in the test. Figure 3 shows the arrangement of the measuring points.
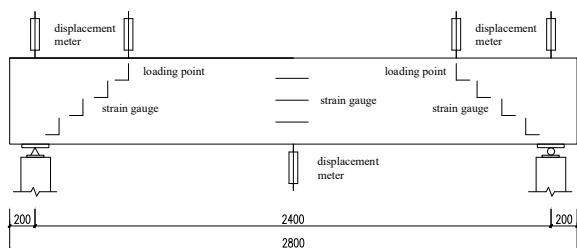

Fig. 3 - Layout of measuring points.

Before the test, the front side of each beam was reserved for displacement measurement of localized zones by digital image correlation (DIC). The DIC is a well-known noninvasive method of velocity measurement. The method was originally developed for fluid mechanics and used to analyze the displacements in tests on soil and rock models [15, 16]. To facilitate real-time measurement, a few dots of proper sizes were marked randomly, and a camera was installed on the front surface of the beam to collect a series of images. The images were then meshed into grids, and compared to track the spatial variation of brightness. The displacements were extracted from the series of meshed images. Finally, the strains were computed from the displacement gradient. The test setup is illustrated in Figure 4 below.

Fig. 4 - Test setup.

3.3. Tests on material properties

(1) Test on concrete properties

According to the *Standard for Test Method of Mechanical Properties on Ordinary Concrete* (GB/T 50081-2002) [17], six test cubes (100mm×100mm×100mm) and nine standard test cubes (150mm×150mm×150mm) were prepared and cured for 28d under the same conditions as the test beams, and used to measure the compressive strength of concrete. Test measured data were processed by the conversion formulas in GB 50010-2010:

$$f_c = 0.76 \times a_2 \times f_{cu} \tag{5}$$

$$f_t = 0.395 \times a_2 \times f_{cu}^{0.55} \tag{6}$$

The final results on the compressive strength of concrete are listed in Table 3.

Table 3

Measured mechanical properties of concrete

concrete grade	f_{cu} (MPa)	f_c (MPa)	f_t (MPa)
C30	32.13	24.42	2.66

(2) Test on reinforcements and stirrup properties
According to the *Metallic Materials-Tensile Testing-Part 1: Method of Test at Room Temperature* (GB/T 228.1-2010) [18], three samples were prepared for longitudinal reinforcement, three for nominal top reinforcement and three for stirrups, and were subjected to material property tests. The yield and ultimate

strength were recorded in each test. The mean value of the data measured in three tests on the same material was taken as the final result of the material. The measured mechanical properties are shown in Table 4.

Table 4
Measured mechanical properties of reinforcements and stirrups

Diameter (mm)	Reinforcement Grade	Yield Strength (MPa)	Ultimate Strength (MPa)	Elastic Modulus (GPa)	Yield Strains (×10⁻³)
6	HPB300	382	525	197.65	1.93
8	HPB300	330	452	173.21	1.91
10	HPB300	288	439	173.36	1.66
10	HRB400	443	564	194.86	2.28
22	HRB400	420	578	205.01	2.05

4. Test Results

During the loading test, the author observed the propagation of original cracks and initiation of new cracks continuously, and recorded the test phenomena in real time. After the specimen stabilized in each loadings stage, the crack appearance and development were marked with a marking pen, and images of the beam cracks were taken by the camera. The cracks generated in the test were plotted on CAD software and analyzed by the DIC.

4.1 Group A (shear span ratio: 2.0)

Beam A-2.0 and beam A'-2.0, respectively reinforced by the CFP and GB 50010-2010, both undergone shear compressive failure. The first bending crack appeared in the pure flexural section of beams A-2.0 and A'-2.0 under the loads of 25kN and 20kN, respectively. With the increase of the load, some new vertical cracks emerged at beam bottom, while the original cracks gradually propagated. After the load reached 85kN, the vertical cracks of the two beams extended obliquely in the shear span. The oblique development deepened when the load increased to 105kN. When the load grew to 225kN, beam A-2.0 saw a long oblique shear crack linking up the loading point to the support, while beam A'-2.0 witnessed many oblique cracks in the shear span. With further increase in the load, the oblique shear crack of beam A-2.0 widened and extended to both sides, while obvious widening was observed in the oblique crack and midspan crack of beam A'-2.0. The oblique cracks of beams A-2.0 and A'-2.0 reached the maximum widths, respectively, under the loads of 310kN and 300kN. Eventually, the concrete in the shear-compression zone of each beam was crushed, i.e. the shear compressive failure took place. Figures 5 and 6 show the ultimate failure and crack distribution of the two beams, respectively.

The crack patterns of the two beams were obtained by the DIC and plotted as Figure 7.
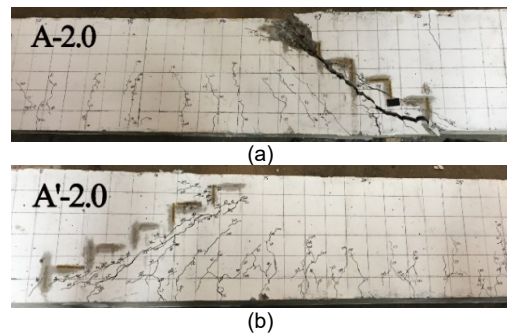

Fig. 5 - Ultimate failures of group A specimens.
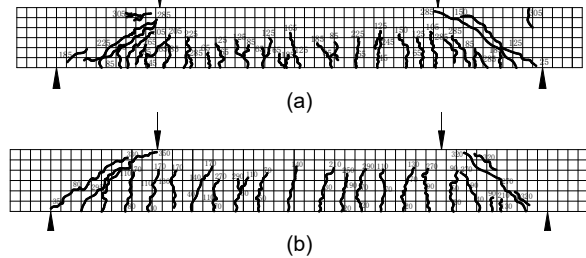(a) Beam A-2.0. (b) Beam A'-2.0.

Fig. 6 - Crack distributions of group A specimens.
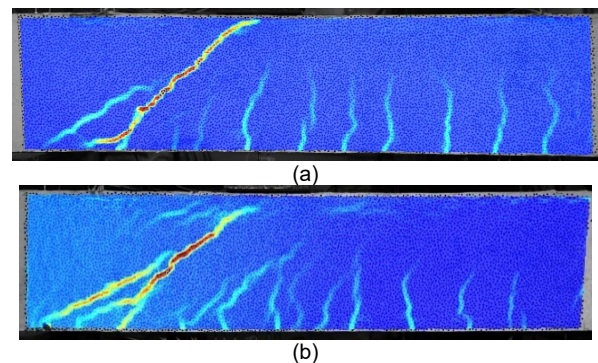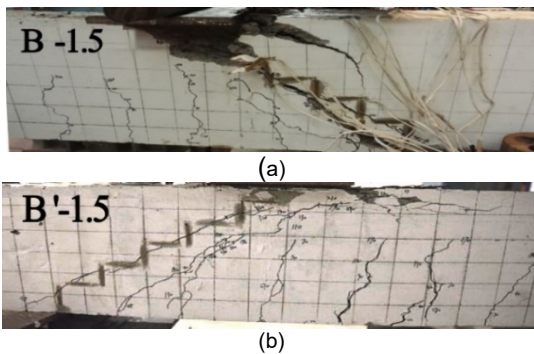(a) Beam A-2.0. (b) Beam A'-2.0.

Fig. 7 - Crack patterns of group A specimens.
(a) Beam A-2.0. (b) Beam A'-2.0.

Comparing the visually-recorded crack pattern (Figures 5 and 6) with the DIC-measured crack pattern (Figure 7), it can be seen that, under the load action, the shear crack propagated clearly from the loading point to the support in the shear span. The crack patterns of beam A-2.0 and beam A'-2.0 agree well with the DIC results under 310kN and 300kN, respectively. The results show that group A specimens undergo shear compressive failure. Compared with those in beam A'-2.0, the crack and strain distributions seen in beam A-2.0 demonstrate the advantages of the CFP method over the GB 50010-2010 in economy and rationality. The advantages come from the relatively small number of stirrups arranged along the CFP in the shear span.

4.2 Group B (shear span ratio: 1.5)

Both beams B-1.5 and B'-1.5 suffered from

shear compressive failures. The first bending crack appeared in the pure flexural section of beams B-1.5 and B'-1.5 under the loads of 20kN and 22kN, respectively. When the load reached about 90kN, the vertical bending crack developed obliquely in the shear span of both beams. The first web shear crack emerged in the shear span as the load grew to 150kN, and started to move to the loading point once the load rose to 330kN. The cracks of beams B-1.5 and B'-1.5 reached the maximum widths, respectively, under 359kN and 384kN, indicating the failure of both beams. Figures 8 and 9 show the ultimate failure and crack distribution of the two beams, respectively.

(a)

(b)
Fig. 8 - Ultimate failures of group B specimens.
(a) Beam B-1.5. (b) Beam B'-1.5.

(a)
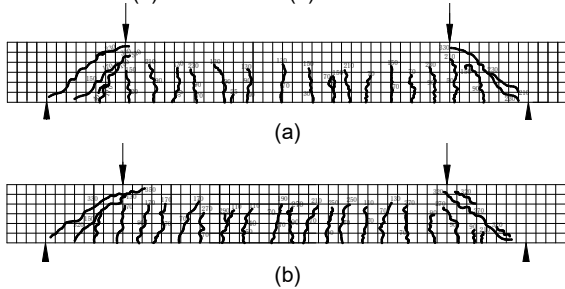
(b)
Fig. 9 - Crack distributions of group B specimens.
(a) Beam B-1.5. (b) Beam B'-1.5.

The crack patterns of the two beams were obtained by the DIC and plotted as Figure 10.
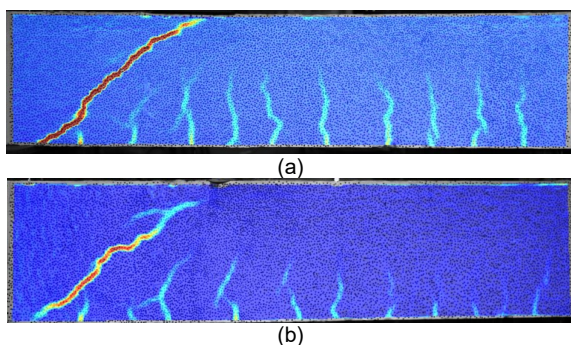

(a)

(b)
Fig. 10 - Crack patterns of group B specimens.
(a) Beam B-1.5. (b) Beam B'-1.5.

Comparing the visually-recorded crack pattern (Figures 8 and 9) with the DIC-measured crack pattern (Figure 10), it can be seen that, under the load action, the shear crack developed all the way from the loading point to the support in the

shear span. The crack patterns of beam B-1.5 and beam B'-1.5 were consistent with the DIC results under 359kN and 384kN, respectively. This means specimens in group B suffered from shear compressive failure. Comparing the crack and strain distributions between the two beams, it is obvious that the CFP method is more economic and rational than the GB 50010-2010. This is because the former method arranges fewer stirrups along the CFP in the shear span than the latter.

4.3 Group C (shear span ratio: 1.0)

Both beams C-1.0 and C'-1.0 ended up in failure under diagonal compression. The two beams started to have vertical cracks in the pure flexural section, once the load increased to about 30kN. With the growth in the load, some new vertical cracks initiated at the beam bottom, while the original cracks continued to extend. Web shear cracks emerged on both beams at the shear span under the load of 200kN, but began to develop differently after the load grew to 400kN. As the load increased to 450kN, quite a few new transverse cracks developed on beam C-1.0 at the support and the area below the loading point, while several fine oblique cracks appeared on beam C'-1.0 below the loading point. The concrete of beams C-1.0 and C'-1.0 was split into oblique short columns and crushed, respectively, under 491kN and 531kN. In the end, both beams suffered from diagonal compressive failure, and the cracks on beam C-1.0 were more developed than those on beam C'-1.0. Figures 11 and 12 show the ultimate failure and crack distribution of the two beams, respectively.
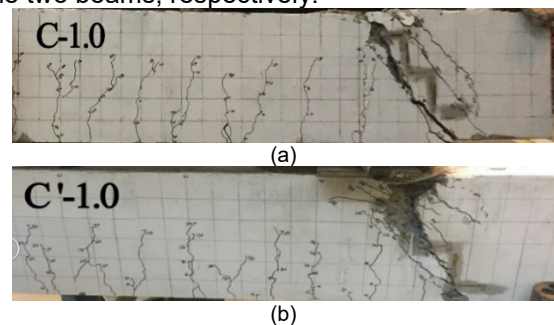

(a)

(b)
Fig. 11 - Ultimate failures of group C specimens.
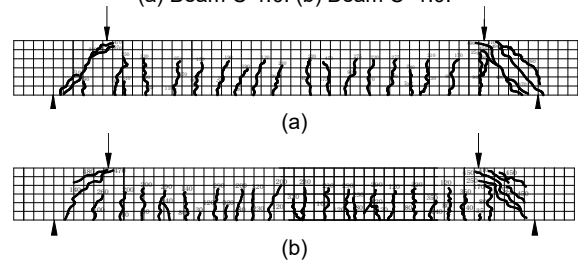(a) Beam C-1.0. (b) Beam C'-1.0.

(a)

(b)
Fig. 12 - Crack distributions of group C specimens.
(a) Beam C-1.0. (b) Beam C'-1.0.

The crack patterns of the two beams were obtained by the DIC and plotted as Figure 10.

Table 5

The main test results

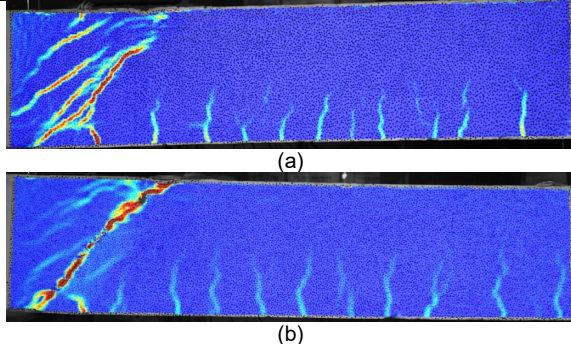| Specimen	A_{sv} (mm²)	P_{cr} (kN)	P_u (kN)	Δ_{u1} (mm)	Δ_u (mm)	Amount of Stirrups Saved by CFP Method	Failure Modes
A-2.0	792.40	25	310.89	15.90	18.80	40%	shear compression
A'-2.0	1320.40	20	303.80	19.00	21.60		
B-1.5	566.00	20	360.00	11.35	15.25	57%	shear compression
B'-1.5	1320.40	22	384.40	11.51	17.74		
C-1.0	566.00	30	491.00	5.98	13.90	68%	diagonal compression

(a)

(b)

Fig. 13 - Crack patterns of group C specimens.
(a) Beam C-1.0. (b) Beam C'-1.0.

Comparing the visually-recorded crack pattern (Figures 11 and 12) with the DIC-measured crack pattern (Figure 13), it can be seen that the load action induced obvious propagation of the shear crack from the loading point to the support in the shear span.The crack patterns of beam C-1.0 and beam C'-1.0 echoed with the DIC results under 491kN and 531kN, respectively, which signified the diagonal compressive failures of group C specimens. From the crack and strain distributions of the two beams, it can be observed that the CFP method outshines the GB 50010-2010 in economy and rationality. This is attributable to the limited number of stirrups arranged along the CFP in the shear span.

5. Discussion

The main test results of the two types of beams are recorded in Table 5, including the shear stirrup area A_{sv}, cracking load P_{cr}, the failure load P_u, the displacement Δ_{u1} at loading point and the maximum displacement Δ_u at midspan.

As shown in Table 5, the CFP beams exhibited shear compressive failure under a slightly lower load (i.e. the cracking load) than GB beams, and had similar midspan displacement with the latter. Group C is an exception: the CFP beams in this group showed greater midspan displacement than that of GB beams. The ultimate loads of the two types of beams are compared in Table 6 below. The number of stirrups saved in each group by the CFP method is also included in the Table.

It can be seen from Figure 6 that the two types of beams had a minor difference in failure load, despite a 40%-68% difference in the number of stirrups. Moreover, the number of stirrups saved by the CFP method is negatively correlated with the shear span ratio.

Table 6

The ultimate loads

Group	Group A 40%	Group B 57%	Group C 68%
CFP (kN)	310	360	491
GB 50010-2010 (kN)	303	384	531

5.1. Shear capacity

Table 7 compares the shear capacity measured in our test with the theoretical shear capacity calculated by the CFP method.

Table 7

Comparison between measured and calculated shear capacities

Specimen	A-2.0	B-1.5	C-1.0
Measured value (kN)	310	360	491
Calculated value (kN)	280	374	561

No marked difference was observed between the measured and calculated shear capacities, except for beam C-1.0. This observation demonstrates the feasibility of the CFP method. In general, the CFP's shear capacity formula achieved a high accuracy in predicting the ultimate load of the simply supported beam. However, the ultimate load was overestimated when the shear span ratio is 1.0. The beams with this shear span ratio failed ultimately under diagonal compression. Thus, their shear capacities should not be analyzed according to the type III failure mode.

5.2. Load-deflection analysis
(1) Load-deflection features of test beams

The load-deflection curves of the specimens in each group are displayed in Figure 14.

In the early stage of loading, there were only microcracks on the specimens. In this case, most of the stress was carried by the concrete, and only a minor fraction was applied on longitudinal reinforcement. With the increase of the load, the initial microcracks gradually developed into main cracks in the beams. In this case, the stirrups gradually replaced the concrete as the main carrier of the shear force. As the load further grew to the ultimate load, the beam deflection continued to increase, and the cracks became increasingly wide. Thus, the longitudinal reinforcement reached its maximum strain or even yielded. In this case,
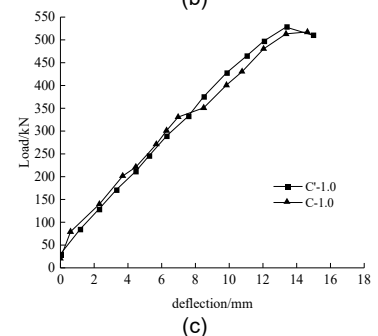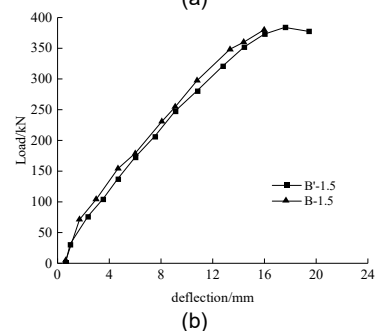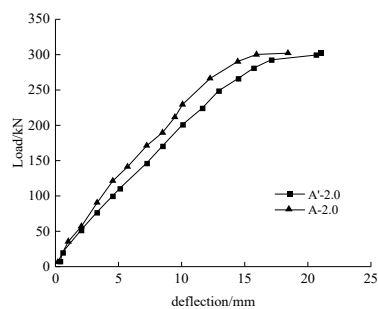
Fig. 15 - The grid meshing of the three CFP beams.

Fig. 14 - Load-deflection curves of specimens.
(a) Group A. (b) Group B. (c) Group C.

Fig. 16 - Simulated and experimental load-deflection curves of
the CFP specimens. (a) Beam A-2.0. (b) Beam B-1.5.
(c) Beam C-1.0.

the beams were clearly deflected and met with eventual failure.

Figure 14 shows that the two types of beams, with significant difference in the number of stirrups, exhibited an unobvious difference in growth trend of the load-deflection curve, and a small disparity in terms of the beam deflection at failure.

(2) Finite-element analysis of the CFP beams

The author set up a finite-element model of the CFP beams on Abaqus. The steel plate at the supports and the loading points were simulated as C3D8R elements, while the reinforcement was modelled as T3D2 elements. In light of the test conditions, the steel plate was tied with the concrete beam; the reinforcement was embedded in the beam under the embedded region constraint; the bond-slip interaction between the steel plate and concrete was so small as negligible [19,20]. The grid meshing of the three CFP beams is described in Figure 15.

Figure 16 compares the simulated load-deflection curves of the three CFP beams are compared with the experimental curves.
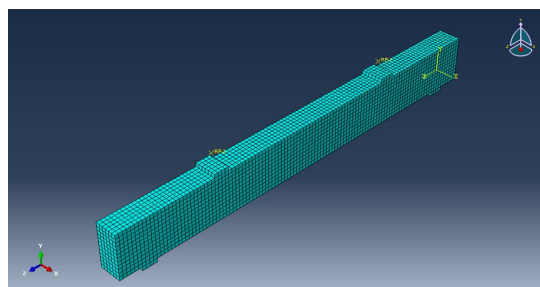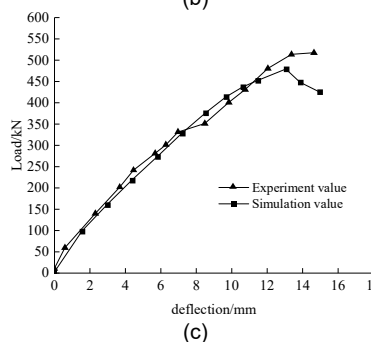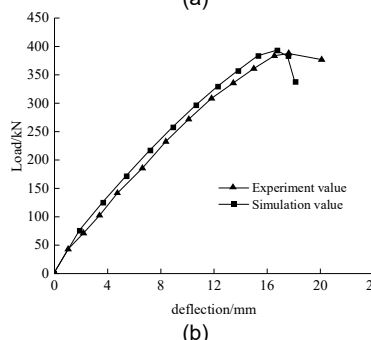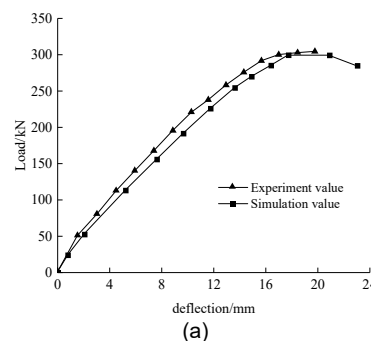
It is evident from Figure16 that the load-deflection curves simulated on Abaqus were basically consistent with the experimental curves, despite a slight disparity. The simulated ultimate loads are contrasted with the measured results in Table 8.

The results in Table 8 show a good resemblance between the simulation and test results on the ultimate loads of the CFP beams. The simulated ultimate loads deviated from the

Table 8
Comparison of the simulated and measured ultimate loads

Specimen	A-2.0	B-1.5	C-1.0
Simulation value (kN)	299	392	478
Experiment value (kN)	310	360	491
Error (%)	3.7	8.2	2.7

measured results by less than 10%, which is obviously acceptable. The comparison reflects that the proposed finite-element model can accurately simulate the mechanical behavior of the test beams, and that the shear capacity computed by the CFP method is rational and feasible.

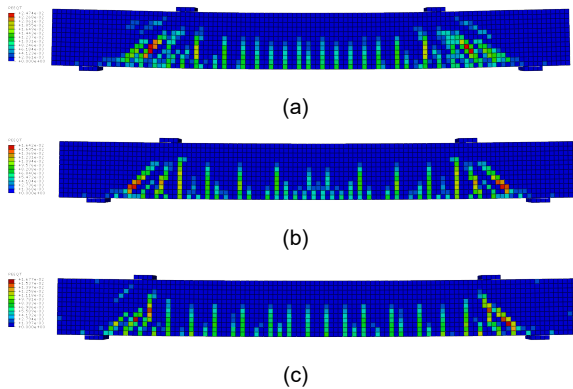### 5.2.3. Simulated crack distributions

(a)

(b)

(c)
Fig. 17 - Crack distributions of CFP beams obtained by finite-element simulation (a) Beam A-2.0. (b) Beam B-1.5. (c) Beam C-1.0.

Figure 17 presents the crack distributions of CFP beams, which illustrate the failure patterns of the beams. The crack distribution was described by equivalent plastic strain. As shown in the figure, both beams A-2.0 and B-1.5 underwent shear compressive failure, while beam C-1.0 failed under diagonal compression. The results are clearly in line with the ultimate failures of the beams, as shown in Figures 5(a), 8(a) and 11(a).

5.3. Strain analysis
(1) Strain in longitudinal reinforcement

As shown in Figure 2, the strain gauges for longitudinal reinforcement were placed at beam midspan, the loading point and the point where longitudinal reinforcement intersects the straight line between the loading point and the support (hereinafter referred to as the intersection point). The gauges at the midspan recorded the strain changes of the reinforcement in the failure process of beams, laying the basis for mechanical analysis.
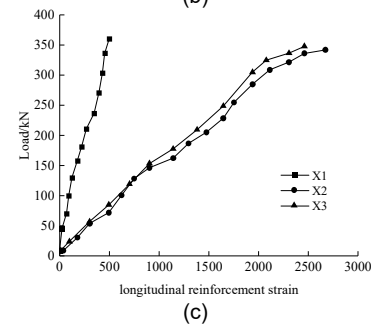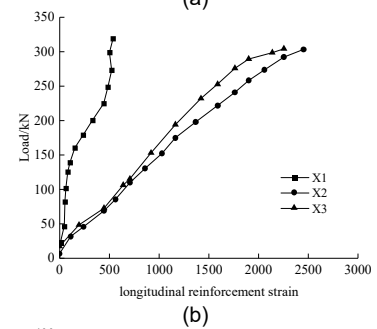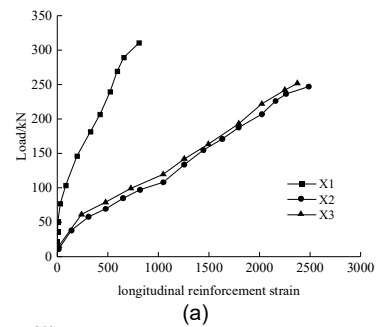
The maximum strains of longitudinal reinforcement under the ultimate loads are listed in Table 9, where ε_1, ε_2 and ε_3 are the strains measured at the intersection point, at the reinforcement just below the loading point, and at the middle of the longitudinal reinforcement.

The maximum strains of longitudinal reinforcement under the ultimate loads are listed in Table 9, where ε_1, ε_2 and ε_3 are the strains measured at the intersection point, at the reinforcement just below the loading point, and at the middle of the longitudinal reinforcement.

Table 9
Maximum strains of the longitudinal reinforcement at the three measuring points

Specimen	$\varepsilon_1/\mu\varepsilon$	$\varepsilon_2/\mu\varepsilon$	$\varepsilon_3/\mu\varepsilon$	Failure Modes
A-2.0	838	2813	2741	shear
A'-2.0	482	2473	3289	compression
B-1.5	901	2689	2218	shear
B'-1.5	710	2593	2698	compression
C-1.0	782	2352	1739	diagonal
C'-1.0	693	1999	2270	compression

The data in Table 9 show that the longitudinal reinforcement at the midspan and below the loading point yielded at the failure of the beam, except in the beams of group C. Under any failure mode, each CFP beam had a smaller longitudinal reinforcement strain than the corresponding GB beam at the midspan, but a greater longitudinal reinforcement strain than the latter under the loading point and at the intersection point. Figure 18 depicts the variation of longitudinal reinforcement strain with loads in each beam.

(a)

(b)

(c)

Ergang Xiong, Kun Zu, Tuanjie Fan, Linbo Liu, Liangying Song, Qian Zhang / Experimental analysis on shear behaviour
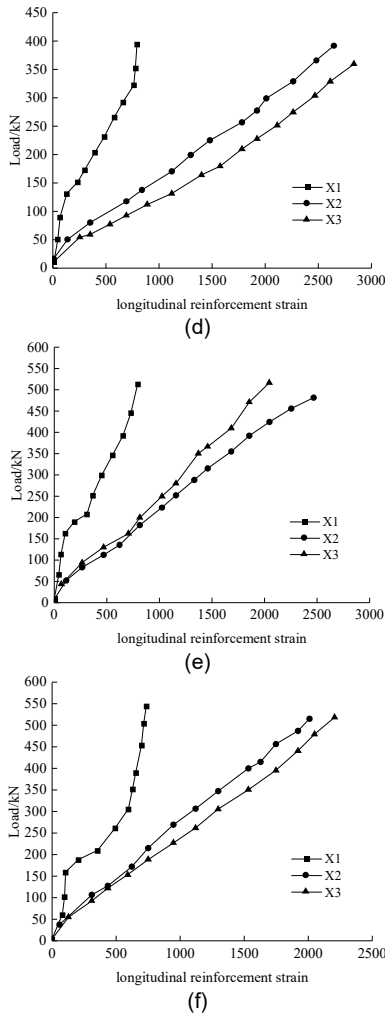of reinforced concrete beams based on compressive force path method
609

Fig. 18 - The variation of longitudinal reinforcement strain with
loads. (a) Beam A-2.0. (b) Beam A'-2.0. (c) Beam B-1.5.
(d) Beam B'-1.5. (e) Beam C-1.0. (f) Beam C'-1.0.

interval of the stirrups in the shear span. In group C, the longitudinal reinforcement strain at the midspan of C-1.0 beam was smaller than that below the loading point, and did not yield when the beam failed under diagonal compressive failure, while that at the midspan of C'-1.0 changed faster than that below the loading point, and ultimately yielded.

(2) Strain in stirrups

In the shear span section of the test beams, strain gauges were arranged inside the 3~5 stirrups along the straight line between the loading point and the support. The specific positions are shown in Figure 2. The load-stirrup strain curves of the test beams are shown in Figure 19.

As shown in Figure 18, the longitudinal reinforcement had a small initial strain at each measuring point, which grew slowly before crack initiation. After vertical cracks appeared in the midspan, the strain of longitudinal reinforcement gradually increased at the middle and below the loading point. When the cracks emerged in the shear span, the stirrups began to carry load and the stress started to shift towards the support. In this case, the longitudinal reinforcement strain soared at the intersection point.

In both types of beams, the longitudinal reinforcement strain varied with loads in a similar trend. When the stress was about to reach the ultimate load, the longitudinal reinforcement strain increased at a faster rate at the intersection point than the other measuring points. In group A, beams A-2.0 and A'-2.0 shared the same growth trend in longitudinal reinforcement strain at the midspan and below the loading point. The only difference is attributable to their different positions and intervals of the stirrups in the shear span. In group B, beam B-1.5 had a slightly greater longitudinal reinforcement strain than B'-1.5 at the intersection point, due to its different position and
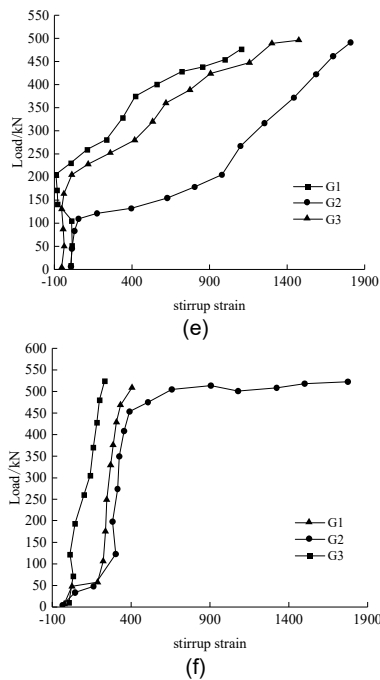
Fig. 19 - Load-stirrup strain curves of test beams. (a) Beam A-2.0. (b) Beam A'-2.0. (c) Beam B-1.5. (d) Beam B'-1.5. (e) Beam C-1.0. (f) Beam C'-1.0.

From Figure 19, it can be seen that the stirrup strain was small, despite the action of compressive stress. Before oblique cracking, the shear force was mainly borne by the concrete rather than the stirrups. When the load reached 30%~40% of the ultimate load, oblique cracks emerged in the shear span section, and the concrete failed. Then, the shear forced was transferred by the stirrups at the intersections of oblique cracks. In this case, the stirrup strain gradually increased in the shear span and near the loading point, but remained small near the support. Since the stirrups restrained the propagation of oblique cracks, the load continued to increase before the stirrups yielded. Under the increasing load, the beam deflected to a greater degree, and the stirrup strain became greater. After the ultimate load was reached, the stirrups in the web of the beam yielded first, and the shear oblique crack extended to the loading point and the support, forming a penetrating oblique crack. Thus, the concrete in the upper shear-compression zone was crushed, and the test beam eventually failed.

It can be seen form Figure 19 that the CFP beams had greater stirrup strains than GB beams in groups A and B, both of which underwent shear compressive failure. The results show that the stirrups played a significant role in controlling crack development. In group C, beam C-1.0 had a greater stirrup strain than beam C'-1.0 in shear span section. Both suffering from diagonal compressive failure, C-1.0 used 68% fewer stirrups than C'-1.0, revealing that the former has a high utilization rate of stirrups.

6. Conclusions

The crack patterns and strain diagram of steel reinforcement were analyzed, revealing that the stirrups along the CFP can effectively restrain the development of oblique cracks. The finding verifies the existence of the CFP. The beams designed by the CFP method achieved the desired shear performance.

The CFP method can accurately compute the ultimate load of beams with shear span ratios of 2.0 and 1.5. For the beams with shear span ratio of 1.0, however, the shear design of RC beams with diagonal compressive failure should not be designed according to the type III failure mode.

Despite using 40%~68% fewer stirrups, the CFP beams achieved comparable or better shear capacity than GB beams. This means the CFP method can satisfy safety requirements with less cost than the deign method in the current Chinese code on concrete design.

REFERENCES

[1] J.Q. Wang, J.N. Qi, Unified Shear Strength Computation Model for Reinforced Concrete Beams with and without Stirrups. China Civil Engineering Journal. 2014, **7**, 47.

[2] T. Zhang, P. Visintin,. D. J. Oehlers, Shear Strength of RC Beams with Steel Stirrups. Journal of Structural Engineering. 2016, **2**, 04015135.

[3] W.W. Wei, J.X. Gong, Shear Strength Prediction of Reinforced Concrete Flexural Members with Stirrups Based on Modified Compression Field Theory. Journal of Building Structures. 2011, **5**, 135-141.

[4] Z. Wang, Master's Thesis, Research on Inclined Section Shear Capacity of Reinforced Concrete Beams. Master's Thesis, Xi'an University of Architecture and Technology, Xi'an, China, 2012.

[5] M.D Kotsovos, Compressive Force Path Concept：Basis for Reinforced Concrete Ultimate Limit State Design. ACI Structural Journal. 1988, **1**, 68.

[6] M.D. Kotsovos, L.D. Lefas, Behavior of Reinforced Concrete Beams Designed in Compliance with the Compressive Force Path. ACI Structural Journal. 1990, **2**, 127.

[7] M.D. Kotsovos, Behavior of Reinforced Concrete Beams with a Shear Span to Depth Ratio between 1.0 and 2.5. ACI Structural Journal. 1984, **3**, 279.

[8] M.D. Kotsovos, Shear Failure of Reinforced Concrete Beams. Engineering Structures. 1987, **1**, 32.

[9] H.H. Zheng, Z. Liu, Z.Q. He, Strut-and-Tie Models for Diaphragms of Concrete Box-Girder Bridges and Reinforcement Design. Engineering Mechanics. 2011, **5**, 97.

[10] Chinese National Standards. GB 50010-2010(2015), Code for Design of Concrete Structures; China Architecture and Building Press: Beijing, China, 2010, 54.

[11] M.P. Nielsen, L.C. Hoang, Limit Analysis and Concrete Plasticity, 3rd ed.; CRC Press: Boca Raton, United States, 2010, 154.

[12] J.P. Zheng, Diagonal Cracking and Shear Strength of Reinforced Concrete Beams. Magazine of Concrete Research 1997, **178**, 55.

[13] M.D. Kotsovos, Compressive force-path method：Unified Ultimate Limit-State Design of Concrete Structures, 1st ed.; Springer International Publishing, Switzerland, 2014, 64.

[14] Chinese National Standards. GB/T 50152-2012, Standard for Test Method of Concrete Structures; China Architecture and Building Press: Beijing, China, 2012, 35.

[15] N. McCormick, J. Lord,. Digital Image Correlation for Structural Measurements. Civil. Eng. 2012, **4**, 185-190.

[16] M. Dutton, W.A. Take, N.A. Hoult, Curvature Monitoring of Beams Using Digital Image Correlation. Journal of Bridge Engineering. 2013, **3**, 185.

[17] Chinese National Standards. GB/T 50081-2002, Standard for Test Method of Mechanical Properties on Ordinary Concrete; China Architecture and Building Press: Beijing, China, 2003, 15.

[18] Chinese National Standards. GB/T 228.1-2010, Metallic Material-Tensile Testing-Part 1: Method of Test at Room Temperature; China Architecture and Building Press: Beijing, China, 2010, 11.

[19] W.J. Deng, Q. Li, Z.C. Xie, P. Lin, Numerical analysis of rectangular groove cutting with different RC tools. International Journal of Simulation Modelling. 2013, **2**, 120.

[20] R. Ahmed, M. Shah, M. Umar, Concepts of simulation model size and complexity. International Journal of Simulation Modelling. 2016, **2**, 213.

****

MANIFESTĂRI ȘTIINȚIFICE / SCIENTIFIC EVENTS

The third RILEM Spring Convention and Conference, RSCC2020, will be organized by the University of Minho, in Guimarães, between the 10th and the 14th of March 2020.
The same event will combine the RILEM standing committee meetings (TAC, DAC, DEV, Bureau), several RILEM technical committee meetings (TC), a PhD Workshop, a Plenary RILEM Workshop and a Conference.

TOPICS
The event theme is closely related to the most critical challenges that humanity currently faces, which relate to RILEM activity. ***"Ambitioning a sustainable future for built environment: comprehensive strategies for unprecedented challenges"***. Under this theme, four main topics are proposed:

Topic 1: Strategies for a resilient built environment
This topic will coverall the aspects related to current and emerging approaches that lead to an optimized design and maintenance of constructions and systems. It includes the development of service life models and life cycle design, in order to maximise longevity and level of service while minimising the environmental impact of constructions and systems. It may include also the analysis and design of larger systems, such as communities, cities or regions, aiming at reducing risk and increasing resilience.

Topic 2: New materials and structures for ultra-durability
This topic will cover the current scientific and technological developments aimed at improving knowledge about degradation mechanisms in construction materials, as well as to the development of new materials with extreme durability. Novel special materials for extreme environments or extreme loading conditions are also included, as well as novel approaches to improve the performance and durability of currently common construction materials. Contributions to this topic are expected to focus primarily at the scale of the materials and their micro-meso-properties.

Topic 3: Service life extension of existing structures:
This topic will cover the most recent scientific and technological developments in the understanding of the evolution and degradation of construction materials and structural systems. Analytical and numerical, as well as experimental approaches, aimed at characterizing, modelling and predicting the evolution of the physical, chemical and mechanical properties of construction materials and structural systems are regarded. Multiphysics models are also considered, as well as other strategies that contribute for an accurate characterization and prediction the service life and the evolution of existing and novel construction materials under normal or extreme environmental exposure or loading conditions. New strategies to promote the smart repairing or the recovery of material properties, as well as the service life extension, are also considered.

Topic 4: Shift to a circular economy
This topic is focussed on sustainability and will cover the research and technology on the use and development of sustainable materials and structural systems, as well as on recycling and reusing. It will also cover the implementation of industrial processes leading to minimized waste, including digital fabrication and deconstruction, as well as integrative approaches that lead to the achievement of the concept of circular economy. Additionally, this topic will cover research on novel or existing construction materials and systems based on local resources and regional practices.

https://www.rscc2020.civil.uminho.pt/event

****